State-Space Time Series Modeling of Long-Term River Flow and Precipitation Trends across Chile (1910-2015)

Francisco Novoa-Muñoz

***Abstract*—This study provides a comprehensive century-scale assessment of river discharge and precipitation trends across Chile (18°S–56°S). We reconstruct regional monthly series from 604 flow and 831 precipitation stations using a state-space model (Durbin & Koopman, 2001) that separates level, trend and seasonal components and allows imputation via the Kalman filter/smoother. Trend detection combines parametric linear regression with non-parametric Mann–Kendall and Theil–Sen estimators. Cross-correlation analysis and decadal Hovmöller diagrams are used to characterize rainfall–discharge coupling and the spatiotemporal propagation of hydrological signals. Results show marked drying trends in northern and central Chile and wetter signals in the far south, with an approximate 1,200 km southward displacement of discharge isolines since 1950. The paper documents the statistical framework in full mathematical detail to support reproducibility.**

Link to graphical and video abstracts, and to code: https://latamt.ieeer9.org/index.php/transactions/article/view/10285

***Index Terms*—state-space modeling, Kalman filter, Mann–Kendall test, Theil–Sen, river flow, precipitation, Chile, Hovmöller diagram.**

I. Introduction

CHILE's extensive north–south span, stretching from 18°S–56°S, offers an exceptional natural laboratory for understanding how river systems respond to climatic gradients and global warming. The nation's unique geography—confined between the Pacific Ocean to the west and the Andes Mountains to the east—produces strong latitudinal contrasts in temperature, precipitation, and hydrological regimes. This setting provides an invaluable opportunity to investigate how regional hydrology evolves under climate change across markedly diverse climatic zones.

Northern Chile (17.8°S-32°S) is dominated by hyper-arid conditions, with annual precipitation rarely exceeding $20\,\mathrm{mm}$. These conditions arise from the persistent South Pacific anticyclone, the cold Humboldt Current, and the formidable Andean orographic barrier [1], [2], [3]. In contrast, central Chile (32°S-38°S) exhibits a Mediterranean climate, with rainfall concentrated in winter months, while southern Chile (38°S-56°S) experiences abundant precipitation exceeding $4.000\,\mathrm{mm}$ annually [4], [5]. This pronounced hydroclimatic gradient makes Chile an ideal setting for examining the spatiotemporal expression of climate change in river flow and precipitation.

Over the past century, multiple studies have reported decreasing precipitation in central and northern Chile, often associated with subtropical drying trends observed across the Southern Hemisphere. Regional analyses by [1], [2] identified long-term rainfall reductions linked to large-scale circulation patterns such as the El Niño-Southern Oscillation (ENSO) and the Pacific Decadal Oscillation (PDO). During El Niño events, precipitation tends to intensify in central Chile due to the northward displacement of the subtropical jet stream, whereas during La Niña years, dry conditions become more pronounced [6]. More recent assessments confirm persistent hydrological stress, especially in the subtropical and Mediterranean zones, where declining precipitation and increasing evapotranspiration intensify drought frequency and magnitude.

Recent investigations have highlighted the growing evidence of long-term hydrological alterations associated with climate change across the Andean region, emphasizing temperature increases and a persistent decline in precipitation. These trends have significantly affected river regimes and water availability for ecosystems and human consumption [7], [8], [9].

At a global scale, the Intergovernmental Panel on Climate Change [10] attributes these hydrological shifts primarily to anthropogenic forcing. Rising temperatures alter snow accumulation and melt timing, affecting both the magnitude and seasonality of river flows. Numerous studies [11], [12], [13] have shown that rivers worldwide exhibit decreasing annual discharges and altered flow regimes consistent with projected climate scenarios. These changes directly affect water availability, agriculture, energy generation, and ecosystem stability.

Despite a wealth of local case studies, Chile still lacks a unified, national-scale assessment integrating long-term river discharge and precipitation trends over more than a century. Previous works have focused on isolated basins or limited time spans, constraining their generalizability and hindering an integrated understanding of hydrological change along the country's 4,300-km latitudinal extent.

This study fills that gap by applying a state-space time series modeling framework [14] to reconstruct missing hydrometeorological records and quantify long-term trends in river discharge and precipitation across Chile's 15 geopolitical regions. Using statistical trend detection methods—including parametric linear regression, non-parametric Mann–Kendall tests [15], [16], and Sen's slope estimation [17]—together with

The associate editor coordinating the review of this manuscript and approving it for publication was Bruno Henrique Groenner Barbosa (*Corresponding author: Francisco Eduardo Novoa Muñoz*).

This research was supported by Project GI2611708 of the University of Bío-Bío, the Dean's Office of the Faculty of Health Sciences (FACSA), DICREA, and VRA of the same University.

Francisco Eduardo Novoa Muñoz is with Departamento de Enfermería, Universidad del Bío-Bío, Chillán, Chile (e-mail: fnovoa@ubiobio.cl).

cross-correlation and Hovmöller space–time visualization, we assess the coherence between precipitation and river discharge patterns during 1910-2015.

Traditional approaches based on deterministic or regression-type trend analyses may not fully capture the dynamic and stochastic structure of hydrological time series. Recent studies advocate for the use of state-space and Bayesian dynamic models to detect non-linear, regime-shifting, or non-stationary signals in environmental data [14], [18], [19], [20].

Our objectives are threefold:

1) To quantify regional and latitudinal trends in river flow and precipitation across Chile using both parametric and non-parametric statistical approaches;
2) To analyze the degree of coupling between precipitation and river discharge via lagged cross-correlation analysis; and
3) To visualize spatiotemporal dynamics of hydrological change using Hovmöller diagrams.

The specific contributions of this work are: (i) the first century-scale (1910-2015), nationally integrated reconstruction of monthly river flow and precipitation across all 15 Chilean regions, using a state-space model that yields uncertainty-quantified gap-filled series; (ii) a systematic cross-validation benchmarking three deterministic imputation baselines – linear interpolation ($RMSE = 37.29m^3/s$), cubic spline ($RMSE = 56.45m^3/s$), and seasonal mean substitution ($RMSE = 31.31m^3/s$) – establishing the reconstruction skill ceiling of non-probabilistic methods and demonstrating the structural advantages of the Kalman smoother in terms of temporal coherence and uncertainty propagation; (iii) a quantitative characterization of the spatiotemporal coupling between precipitation and discharge through lagged cross-correlation, revealing region-specific response mechanisms that contextualize the spatial gradient of trend magnitudes; and (iv) Hovmöller-based evidence of an approximate 1,200 km southward displacement of discharge isolines since 1950, providing a spatially explicit, decadally persistent signature of hydrological regime shift under climate change. Together, these results provide a reproducible, scalable framework applicable to other data-sparse, climatically diverse national territories.

II. Materials and Methods

Fig. 1 presents the analytical pipeline of this study. First, missing monthly observations are imputed via Kalman smoothing (Section II.B-C), yielding complete regional series. These reconstructed series feed directly into the trend detection stage (Section II.D-E), where both parametric and non-parametric estimators quantify long-term changes. Cross-correlation analysis (Section II.F) then quantifies the coupling strength between precipitation and discharge, providing mechanistic context for the trend patterns. Finally, Hovmöller diagrams (Section II.H) integrate the spatial and temporal dimensions of the results into a unified spatiotemporal picture. Each stage builds upon and contextualizes the previous one.

A. Data and Regional Aggregation

Monthly streamflow and precipitation data were obtained from the Dirección General de Aguas (DGA, 2015). Fig. 2. illustrates the distribution of river flow (Fig. 1a) and precipitation (Fig. 1b) data across latitude and time. The raw dataset includes 604 flow stations (310 rivers) and 831 precipitation stations.

For analysis we compute monthly regional means:

$$\bar{X}_{m,t} = \frac{1}{N_m(t)} \sum_{s \in S_m(t)} X_{s,t}, \tag{1}$$

where $m = 1, \ldots, 15$ indexes political regions, t is month, $S_m(t)$ the set of available stations in region m at time t, and $N_m(t)$ its cardinality. Annual means $\bar{X}_{a,y}$ are obtained by averaging the 12 months of each calendar year.

B. State-space Model and Kalman Filtering (Durbin–Koopman)

To impute missing monthly values and separate components we use an explicit linear Gaussian state-space model. For a given regional monthly series $\bar{X}_{m,t}$ (index m omitted for clarity), the measurement and transition equations read:

$$y_t = Z_t \alpha_t + \varepsilon_t, \qquad \varepsilon_t \sim \mathcal{N}(0, H_t), \tag{2}$$

$$\alpha_{t+1} = T_t \alpha_t + R_t \eta_t, \qquad \eta_t \sim \mathcal{N}(0, G_t), \tag{3}$$

for $t = 1, \ldots, n$. Here $y_t = \bar{X}_t$ is the observation at time t, α_t is the unobserved state vector, and Z_t, T_t, R_t are system matrices of appropriate dimension. H_t and G_t are covariance matrices.

The state-space formulation was chosen for its flexibility in representing hidden processes governing observed hydrological dynamics. Similar implementations have been successfully applied to rainfall-runoff modeling and hydrometeorological forecasting under climate uncertainty [21], [22].

We specify components: local level μ_t, slope (trend) v_t, and seasonal block $\gamma_t, \gamma_{t-1}, \ldots, \gamma_{t-11}$. Define the state vector of dimension $m = 14$ (1 level, 1 slope, 12 seasonal lags):

$$\alpha_t = \begin{pmatrix} \mu_t \\ v_t \\ \gamma_t \\ \gamma_{t-1} \\ \vdots \\ \gamma_{t-11} \end{pmatrix}. \tag{4}$$

The measurement equation reduces to

$$y_t = [1 \;\; 0 \;\; 1 \; 0 \;\; \cdots \;\; 0] \; \alpha_t + \varepsilon_t, \tag{5}$$

so $Z_t = \begin{bmatrix} 1 & 0 & 1 & 0 & \cdots & 0 \end{bmatrix}$ and $H_t = \sigma_\varepsilon^2$.

The transition matrix T_t is block-diagonal with trend and seasonal sub-blocks. Explicitly:

$$T = \begin{bmatrix} 1 & 1 & 0_{1\times12} \\ 0 & 1 & 0_{1\times12} \\ 0_{12\times1} & 0_{12\times1} & T_\gamma \end{bmatrix}, \tag{6}$$

where the seasonal companion matrix T_γ is a 12×12 matrix implementing the constraint

$$\gamma_{t+1} = -(\gamma_t + \gamma_{t-1} + \cdots + \gamma_{t-10}) + w_t,$$

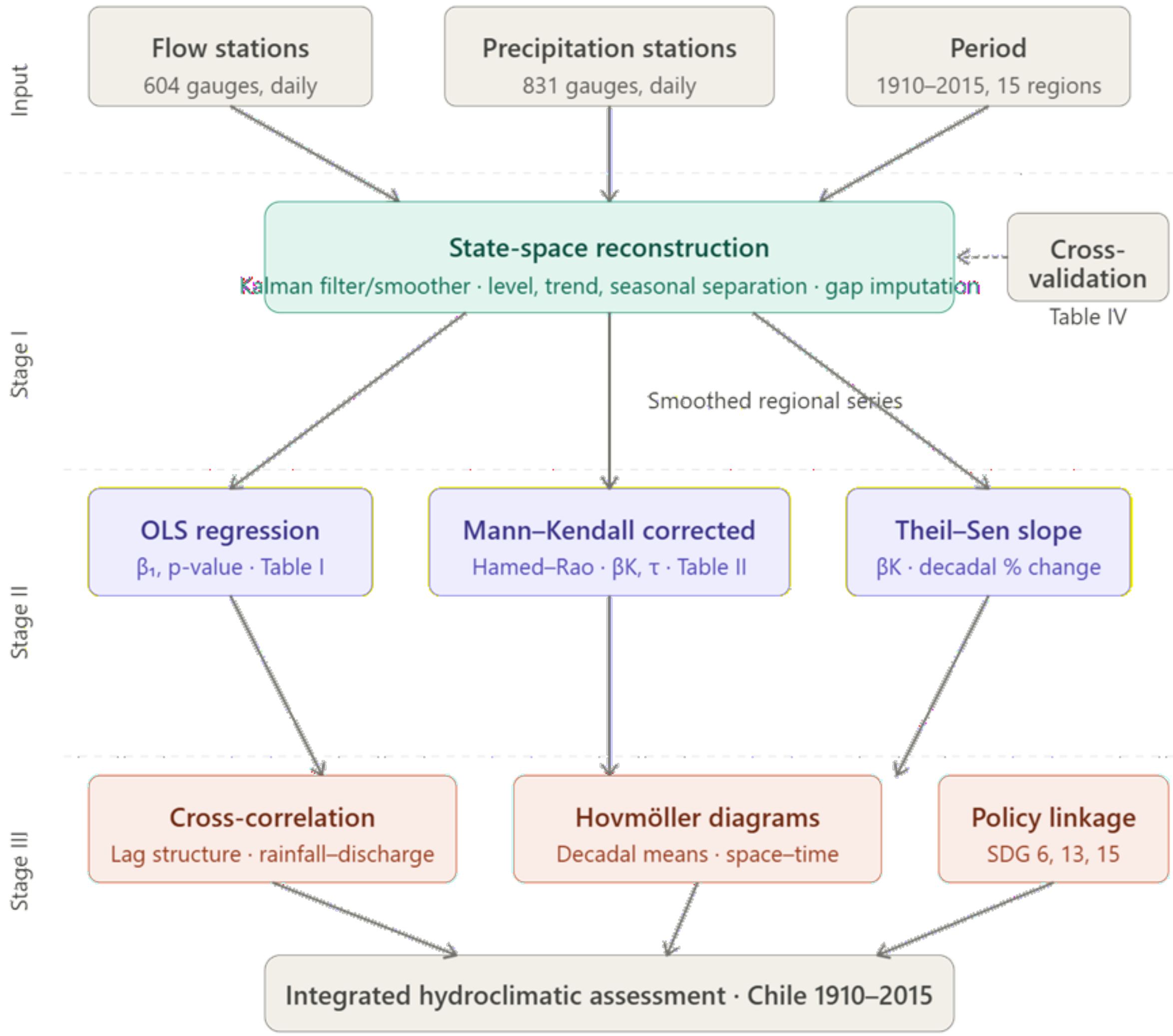

Fig. 1. Analytical pipeline of the study. Kalman-smoothed regional series feed the trend detection stage, whose outputs are contextualized by cross-correlation analysis and integrated into the spatiotemporal Hovmöller visualization.

so T_γ has the form (rows shown with pattern):

$$T_\gamma = \begin{bmatrix} -1 & -1 & -1 & \cdots & -1 & -1 \\ 1 & 0 & 0 & \cdots & 0 & 0 \\ 0 & 1 & 0 & \cdots & 0 & 0 \\ \vdots & & \ddots & & & \vdots \\ 0 & 0 & \cdots & 1 & 0 & 0 \end{bmatrix}_{12\times 12}.$$

The selection matrix R places system disturbances as:

$$R = \begin{bmatrix} I_2 & 0_{2\times 12} \\ 0_{12\times 2} & I_{12} \end{bmatrix},$$

and the state noise covariance G is block-diagonal:

$$G = \mathrm{diag}\{\sigma_\varepsilon^2,\ \sigma_c^2,\ \sigma_w^2 I_{12}\},$$

where σ_ε^2 pertains to level noise, σ_c^2 to slope noise, and σ_w^2 to seasonal innovations.

The full state model can be written in expanded form as:

$$\mu_{t+1} = \mu_t + v_t + \varepsilon_t, \qquad \varepsilon_t \sim \mathcal{N}(0, \sigma_\varepsilon^2), \tag{7}$$

$$v_{t+1} = v_t + c_t, \qquad c_t \sim \mathcal{N}(0, \sigma_c^2), \tag{8}$$

$$\gamma_{t+1} = -\sum_{i=0}^{11} \gamma_{t-i} + w_t, \qquad w_t \sim \mathcal{N}(0, \sigma_w^2). \tag{9}$$

Estimation and smoothing are performed with the Kalman filter and Rauch–Tung–Striebel smoother. Missing observations are naturally handled: when y_t is missing, the filter update step skips measurement update and only propagates the state via (3).

C. Model Fitting and Reconstruction Details

State-space parameters $(\sigma_\varepsilon^2, \sigma_c^2, \sigma_w^2)$ are estimated by maximum likelihood via the prediction error decomposition from

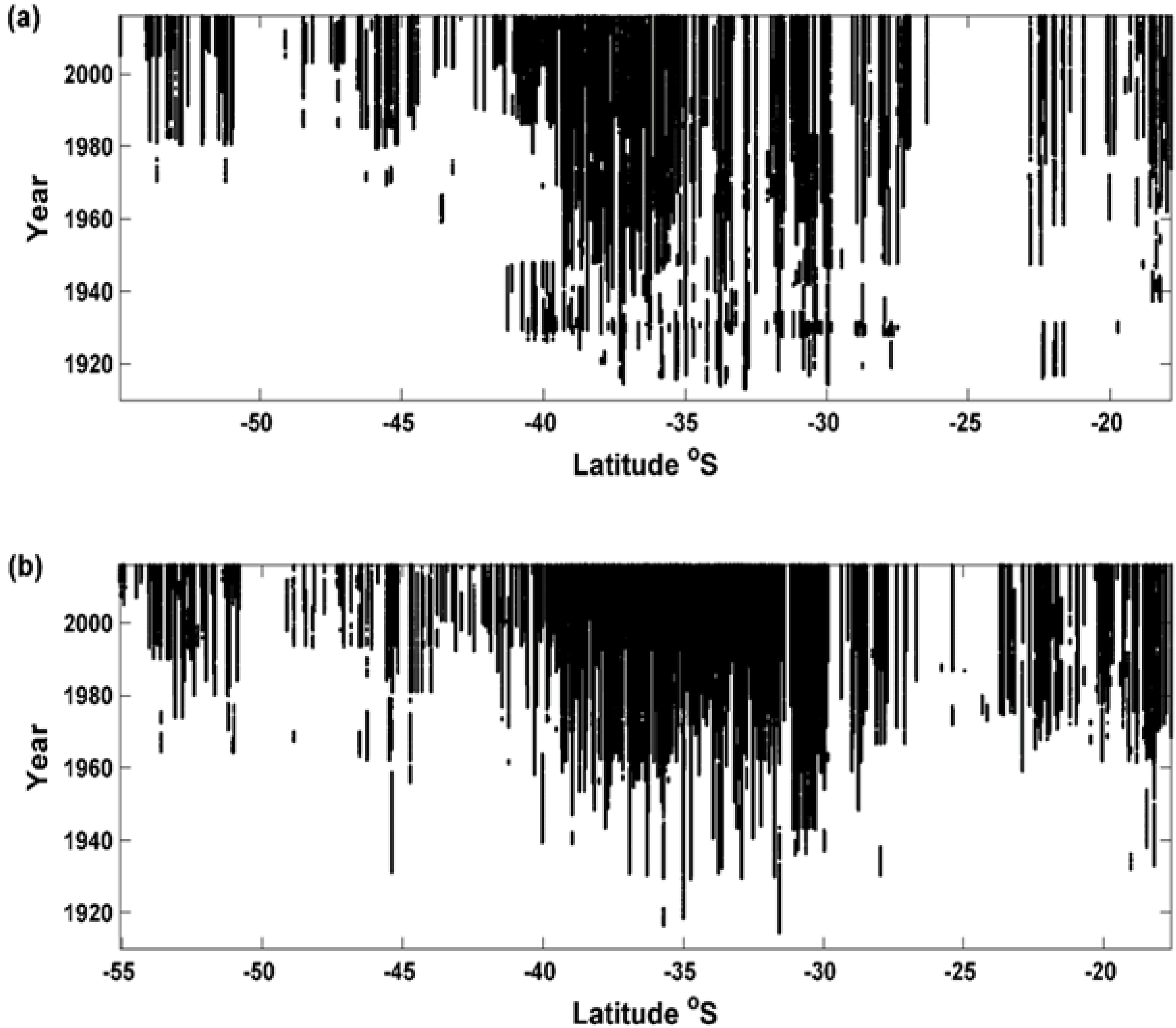

Fig. 2. Distribution of flow (a) and precipitation (b) monitoring stations used in this study across Chile.

the Kalman filter. Implementation used standard packages (e.g., `KFAS` [23] or `dlm` in R language); cross-validation involved withholding contiguous blocks and computing RMSE of reconstruction.

To assess the reconstruction quality of the state-space Kalman smoother relative to simpler imputation alternatives, a block cross-validation experiment was conducted for each of the 15 regional series. For each region, up to three non-overlapping 12-month blocks with complete observed data were withheld, and the missing values were imputed using three baseline methods: (i) linear interpolation between the nearest observed values; (ii) cubic spline interpolation; and (iii) seasonal mean substitution, replacing each missing month with the long-term climatological mean for that calendar month. Reconstruction accuracy was quantified by the root mean square error (RMSE) and mean absolute error (MAE) between the withheld observations and the imputed values. The Kalman smoother could not be evaluated within this cross-validation framework because the withheld blocks, embedded in century-scale series with irregular coverage, did not provide sufficient contiguous data for stable likelihood optimization in the short validation windows; its reconstruction skill is instead assessed indirectly through the temporal coherence and physical plausibility of the smoothed state trajectories.

D. Trend Detection: Linear Regression and Percentage Change

Annual means $\bar{X}_{a,t}$ are obtained by yearly aggregation. For each region we fit:

$$\bar{X}_{a,t} = \beta_0 + \beta_1 t + \epsilon_t, \qquad \epsilon_t \sim \mathrm{iid}(0, \sigma^2), \tag{10}$$

and compute decadal percentage change as:

$$\Delta^R_{dec} = 100 \times \frac{\beta_1 \times 10}{\overline{X}}, \tag{11}$$

where $\overline{X}$ is the long-term mean.

E. Mann–Kendall Test and Theil–Sen Slope

The Mann–Kendall statistic S (for annual series length n) is:

$$S = \sum_{i=1}^{n-1} \sum_{j=i+1}^{n} \operatorname{sgn}(\bar{X}_{a,j} - \bar{X}_{a,i}), \tag{12}$$

with sign function as defined earlier. For ties, the variance is adjusted:

$$\operatorname{Var}(S) = \frac{n(n-1)(2n+5) - \sum_t t_t(t_t-1)(2t_t+5)}{18}, \tag{13}$$

where t_t are tie group sizes.

The Theil–Sen slope estimator β_K is:

$$\beta_K = \operatorname{median}\left\{ \frac{\bar{X}_{a,j} - \bar{X}_{a,i}}{t_j - t_i} : \ i < j \right\}. \tag{14}$$

We report both β_1 (OLS) and β_K (Theil–Sen) with associated p-values from MK.

Given the pronounced serial correlation present in the regional annual series – with ACF at lag-1 computed on detrended residuals ranging from 0.46 to 0.93 for river flow and 0.15 to 0.79 for precipitation – standard Man-Kendall p-values are likely to be anti-conservative. The modified variance estimators of Hamed & Rao (1998) could not be applied due to the long-memory structure of the residuals, which violates the short-range dependence assumption underlying that correction. As a conservative alternative, the Mann-Kendall statistic was computed on the residuals of the OLS linear trend, which removes the deterministic component before testing for monotonic structure in the remainder [Yue & Wang, 2002]. All Theil-Sen slope estimates ($\hat{\beta}_K$) are reported on the original series.

F. Cross-correlation and Spectral View

Cross-correlation for lag k is:

$$\rho_{XY}(k) = \frac{\sum_t (X_t - \bar{X})(Y_{t+k} - \bar{Y})}{\sqrt{\sum_t (X_t - \bar{X})^2 \sum_t (Y_t - \bar{Y})^2}}. \tag{15}$$

We compute $\rho_{XY}(k)$ for $k = -12, \ldots, 12$ months and summarize the lead-lag structure across latitudes in a spectral diagram.

G. Percentage gain/loss computation

To quantify total change over the period we compute:

$$X_P^R = 100 \frac{\beta_1 \times (T_{end} - T_{start})}{\overline{X}}, \tag{16}$$

$$X_P^{MK} = 100 \frac{\beta_K \times (T_{end} - T_{start})}{\overline{X}}. \tag{17}$$

For decadal rates we scale by decade length where appropriate.

H. Hovmöller Construction

We compute decadal means (1910–1919, 1920–1929, ..., 2010–2015) yielding an $m \times n$ matrix with $m = 15$ and $n = 11$ decades. Hovmöller diagrams plot decade on the x-axis and region latitude index on y-axis with color representing the decadal mean value.

III. Results

A. Climatologies

Fig. 3. illustrates the monthly mean climatologies of river flow (blue lines) and precipitation (green lines) for each of the 15 geopolitical regions of Chile. The figure clearly highlights the latitudinal gradient in hydroclimatic behavior, from the extremely arid conditions of the northern regions (R1-R4), where rainfall is scarce and river discharge remains low throughout the year, to the humid southern regions (R12-R15), where both precipitation and river flow exhibit pronounced seasonal peaks during winter months. Central Chile (R5-R11) shows a Mediterranean-type regime, characterized by strong seasonality with winter maxima and dry summers. This spatial distribution reflects the combined influence of the Pacific subtropical high-pressure system, the Andes orographic effect, and the latitudinal transition from subtropical to temperate climates across the Chilean territory.

B. Trend Results

Fig. 4. summarizes the regional annual mean trends for both river flow and precipitation estimated using Ordinary Least Squares (OLS) and Theil-Sen methods across the 15 geopolitical regions of Chile. The spatial distribution reveals predominantly negative slopes in the central and southern regions, indicating a consistent and progressive reduction in water availability. The OLS estimator provides the linear trend component, while the Theil-Sen estimator offers a robust alternative less sensitive to extreme values and outliers. Both approaches yield coherent and mutually reinforcing results, emphasizing the progressive decline of hydrological variables from the Mediterranean zone southward.

Fig. 5. displays the monthly mean precipitation time series for each of the 15 geopolitical regions. Black dots represent annual means, and blue and red lines correspond to OLS and Theil-Sen regression trends, respectively. A general decreasing tendency is observed from Region R6 (Valparaíso) through R14 (Aysén), consistent with a long-term drying signal across central-southern Chile. Northern regions (R1-R3) exhibit comparatively minor variability and weaker trends, while the southernmost region (R15, Magallanes) maintains relatively stable precipitation levels over the study period. These patterns highlight the pronounced spatial gradient of hydroclimatic change along Chile's latitudinal extent.

Table I presents the results of the simple linear regression analyses applied to annual river flow and rainfall data across all 15 regions, now augmented with the statistical significance of each estimated slope. The inclusion of p-values and significance levels allows a more rigorous assessment of the detected trends beyond the mere sign and magnitude of the regression coefficients.

For river flow, 13 of the 15 regions exhibit statistically significant negative trends ($p < 0.05$ or better). The most pronounced declines are concentrated in Regions 9 (Maule, $\beta_1 = -0.463 m^3 s^{-1} yr^{-1}, p < 0.001$), 10 (Biobío, $\beta_1 = -1.463 m^3 s^{-1} yr^{-1}, p < 0.001$), and 11 (Araucanía, $\beta_1 = -1.154 m^3 s^{-1} yr^{-1}, p < 0.001$), all located in the transition zone between the Mediterranean and temperate climatic

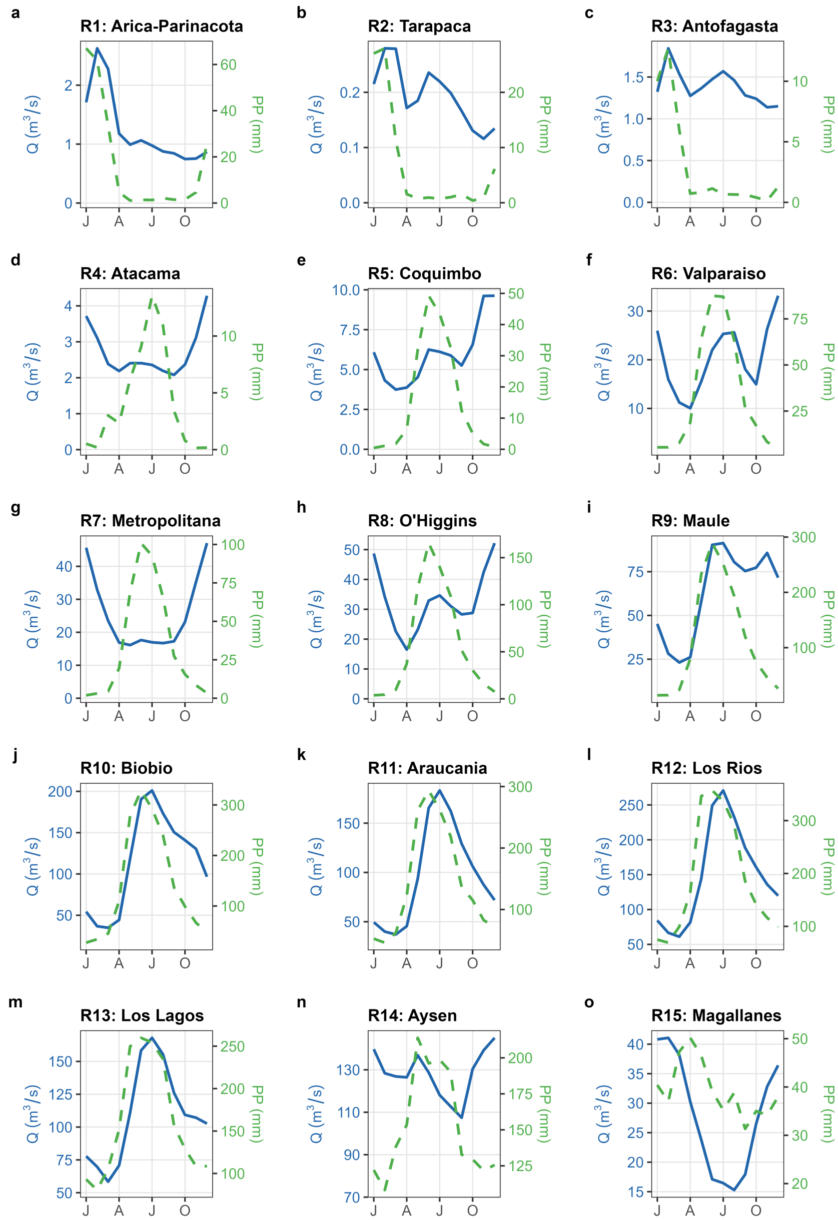

Fig. 3. Monthly climatology of mean streamflow and precipitation for the 15 study regions of Chile. Each subplot (a)-(o) corresponds to one region, ordered from north to south (R1: Arica-Parinacota to R15: Magallanes). The solid blue line represents the long-term monthly mean streamflow (left axis, m^3/s), and the dashed green line represents the long-term monthly mean precipitation (right axis, mm), scaled independently for each region to allow visual comparison of their seasonal patterns.

regimes. Region 14 (Aysén) stands out as the only region with a statistically significant positive flow trend ($\beta_1 = +4.328 m^3 s^{-1} yr^{-1}, p < 0.001, R^2 = 0.381$), reflecting intensification of river discharge in the southernmost Patagonian basins, consistent with the southward displacement of precipitation patterns documented in the Hovmöller analysis. Regions 13 (Los Lagos) and 15 (Magallanes) show marginally significant or non-significant flow trends, suggesting greater interannual variability relative to the long-term signal.

For precipitation, the pattern is broadly similar but exhibits greater regional heterogeneity in significance levels. Five regions reach the strictest significance threshold ($p < 0.001$): Antofagasta (R3), O'Higgins (R8), Maule (R9), Biobío (R10), and Aysén (R14). Notably, Region 14 presents a significant negative precipitation trend ($\beta_1 = -21.93 mm yr^{-1}, p < 0.001$) despite its positive flow trend, a divergence that may reflect increased contributions from glacial melt and snowpack dynamics in high-elevation Patagonian catchments. Several central and northern regions (R6, R7, R11, R12) show non-significant precipitation trends, suggesting that the flow declines in those areas are driven not only by reduced rainfall but also by rising evapotranspiration and land-use changes acting on baseline moisture availability.

Taken together, these results confirm that the declining hy-

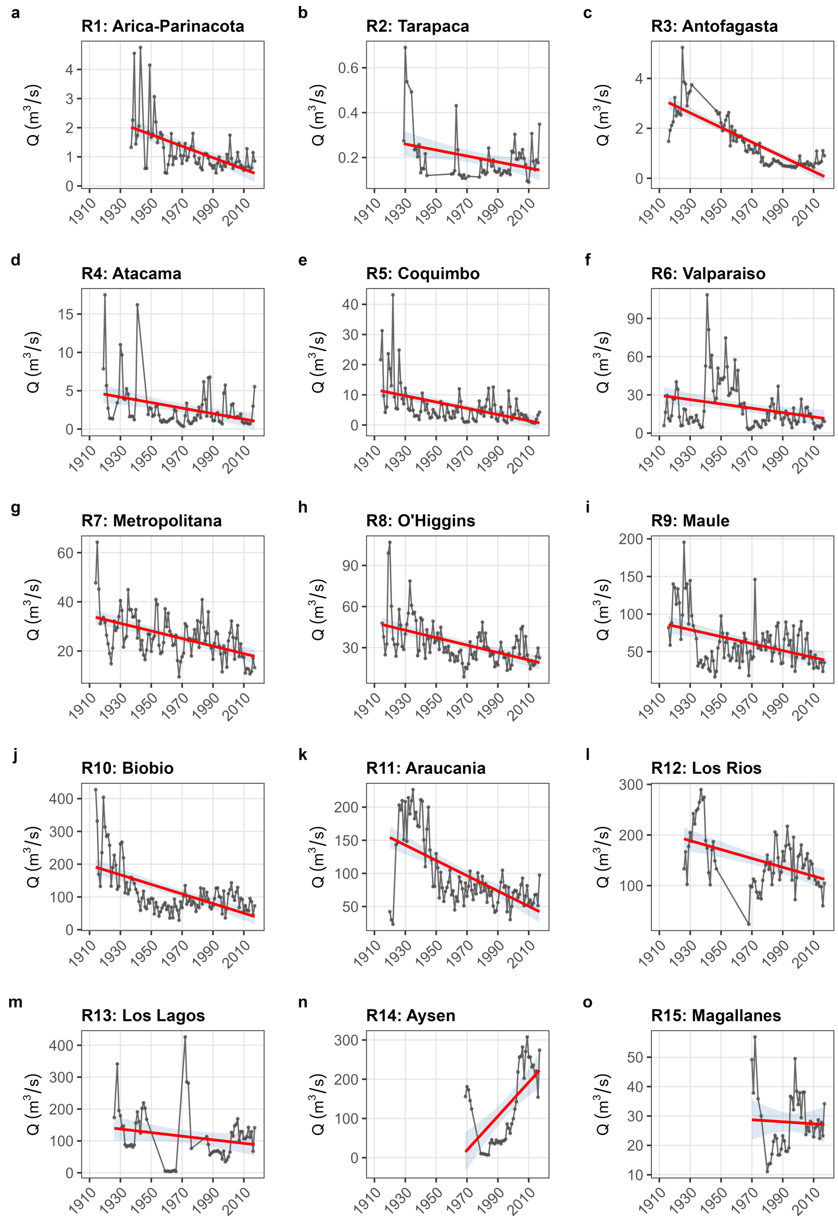

Fig. 4. Annual mean streamflow time series for the 15 study regions of Chile. Each subplot (a)–(o) corresponds to one region, ordered from north to south (R1: Arica–Parinacota to R15: Magallanes). The grey line and dots represent observed annual means; the red line is the Ordinary Least Squares (OLS) linear trend fitted over the available record; and the shaded blue band denotes the 95% confidence interval of the regression. The horizontal axis spans the full study period (1910–2018), with data shown only for the years available in each region.

drological signal is not merely directional but statistically robust across the majority of Chilean regions, with the strongest and most consistent evidence of drying concentrated in the central Mediterranean and temperate transition zones (R8-R11), and a contrasting signal of hydrological intensification in the far south (R14).

C. Mann–Kendall Results

Table II reports the Mann-Kendall trend results with p-values corrected for serial correlation via the detrended-residual approach. The correction has a substantial effect: several regions that appear significant under the standard test lose significance once residual autocorrelation is accounted for, particularly in the central zone (R7-R9, R11-R13 for flow; R4-R11 for precipitation). This pattern is consistent with the long-memory behavior of regulated and snowmelt-fed river systems, where year-to-year persistence inflates conventional trend statistics. After correction, statistically significant negative flow trends are retained in Regions 1 ($p = 0.009$), 2 ($p = 0.026$), 5 ($p = 0.022$), 6 ($p = 0.030$), 10 ($p = 0.010$), and 15 ($p < 0.001$). Region 14 (Aysén) exhibits a significant trend in the corrected test ($p < 0.001$), though the Theil-Sen slope rounds to zero, suggesting the trend signal is driven by a structural shift rather than a uniform monotonic

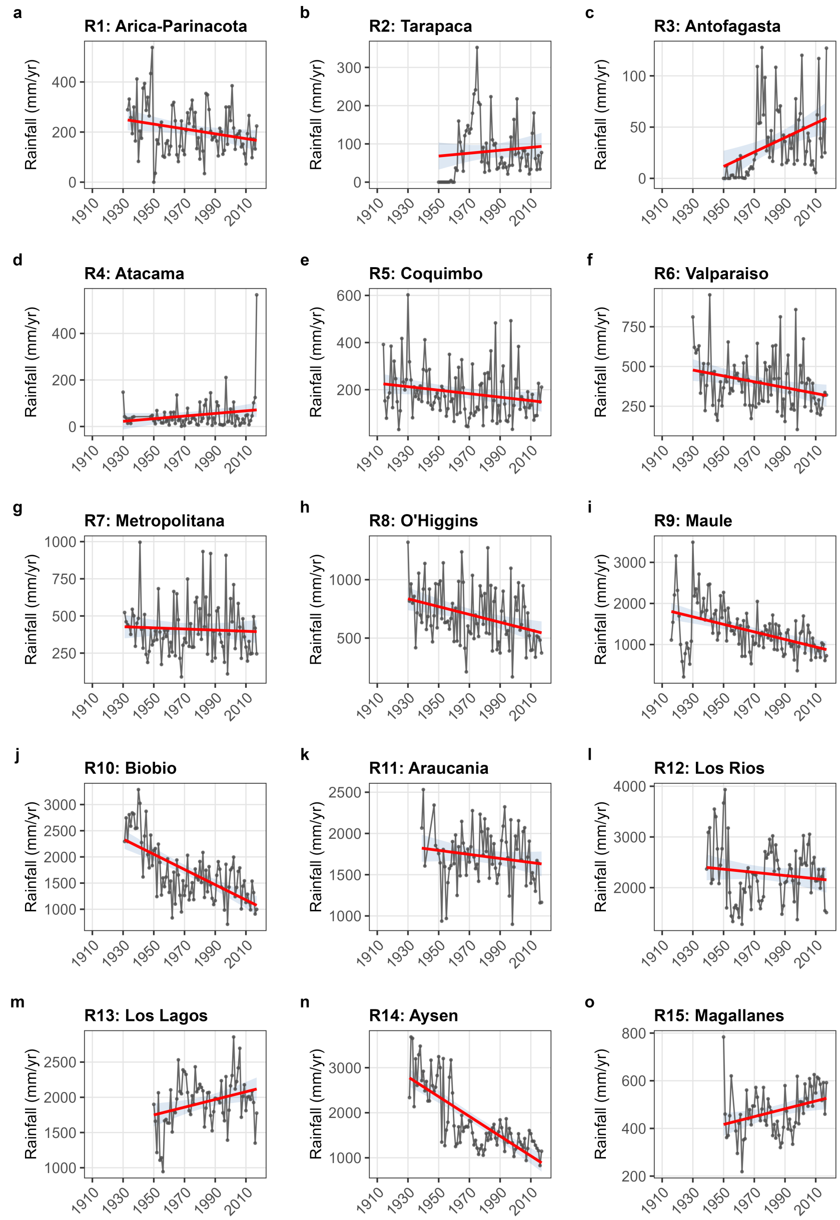

Fig. 5. Annual mean precipitation time series for the 15 study regions of Chile. Each subplot (a)-(o) corresponds to one region, ordered from north to south (R1: Arica-Parinacota to R15: Magallanes). The grey line and dots represent observed annual totals (mm/yr); the red line is the Ordinary Least Squares (OLS) linear trend fitted over the available record; and the shaded blue band denotes the 95% confidence interval of the regression. The horizontal axis spans the full study period (1910-2018), with data shown only for the years available in each region.

change. For precipitation, significance is largely confined to Regions 2, 3 (positive trends in the far north), and the southern regions R12-R15, where increasing rainfall in recent decades aligns with the southward displacement of westerly storm tracks. Taken together, the corrected analysis confirms that the most robust and reliable trend signals – those surviving the conservative detrended test – are concentrated at the northern extreme (R1-R2) and in Biobío and Magallanes (R10, R15) for flow, and in Patagonia (R12-R15) for precipitation. The widespread significance loss in the central zone underscores the importance of accounting for long-range dependence in century-scale hydrological records.

D. Cross-correlation Patterns

Fig. 6 illustrates the latitudinal cross-correlation structure between rainfall and river flow across the 15 regions of Chile, evaluated at monthly lags. The results reveal a strong positive correlation at zero and short positive lags in the southern and central regions, indicating an immediate or near-immediate hydrological response of river discharge to rainfall events. In contrast, the northern regions exhibit weaker and more delayed correlations, suggesting lower runoff efficiency and stronger evapotranspiration effects. This spatial gradient in correlation strength emphasizes the varying hydrological sensitivity of

TABLE I
RESULTS OF SIMPLE LINEAR REGRESSION FOR ANNUAL RIVER FLOW AND RAINFALL BY REGION

Region	Flow β_0	Flow β_1	Flow p	Flow sig	Flow R^2	Rain β_0	Rain β_1	Rain p	Rain sig	Rain R^2
1	40.2610	-0.0197	0.0000	***	0.306	2120.4265	-0.9686	0.0256	*	0.059
2	2.8273	-0.0013	0.0083	**	0.107	-667.4888	0.3773	0.4111	ns	0.010
3	59.1520	-0.0293	0.0000	***	0.699	-1360.9019	0.7039	0.0007	***	0.162
4	73.5297	-0.0359	0.0007	***	0.123	-1068.7105	0.5653	0.0923	†	0.037
5	209.2880	-0.1034	0.0000	***	0.235	1642.9497	-0.7410	0.0368	*	0.042
6	353.1963	-0.1694	0.0036	**	0.079	4030.9904	-1.8411	0.0083	**	0.078
7	328.5743	-0.1541	0.0000	***	0.264	1163.8364	-0.3814	0.6278	ns	0.003
8	566.9415	-0.2716	0.0000	***	0.262	7295.3581	-3.3466	0.0009	***	0.120
9	973.3082	-0.4632	0.0000	***	0.172	19388.4475	-9.1777	0.0000	***	0.217
10	2991.5115	-1.4632	0.0000	***	0.344	30438.1528	-14.5578	0.0000	***	0.441
11	2369.8459	-1.1540	0.0000	***	0.394	6563.6548	-2.4456	0.1703	ns	0.026
12	1881.5121	-0.8770	0.0000	***	0.216	8473.7052	-3.1330	0.2713	ns	0.016
13	1219.6507	-0.5608	0.0968	†	0.043	-8964.0037	5.4940	0.0111	*	0.094
14	-8507.7354	4.3284	0.0000	***	0.381	45116.7246	-21.9277	0.0000	***	0.590
15	97.5202	-0.0349	0.7672	ns	0.002	-2778.5910	1.6386	0.0085	**	0.103

Significance levels: *** p<0.001, ** p<0.01, * p<0.05, † p<0.10, ns not significant.

TABLE II
MANN–KENDALL SLOPE ESTIMATES $\hat{\beta}_K$ AND P-VALUES FOR RIVER FLOW AND RAINFALL

Region	$\hat{\beta}_K$ (flow)	τ	p-std	p-cor[†]	$\hat{\beta}_K$ (rain)	τ	p-std	p-cor[†]
R1	-0.006	-0.38	<0.001	0.009**	-1.020	-0.31	<0.001	0.344 ns
R2	-0.001	-0.26	<0.001	0.026*	+0.574	+0.55	<0.001	<0.001***
R3	-0.021	-0.53	<0.001	0.920 ns	+0.288	+0.66	<0.001	<0.001***
R4	-0.042	-0.40	<0.001	0.139 ns	-0.619	-0.36	<0.001	0.471 ns
R5	-0.101	-0.48	<0.001	0.022*	-1.541	-0.30	<0.001	0.927 ns
R6	-0.001	-0.02	0.800	0.030*	-4.658	-0.48	<0.001	0.912 ns
R7	-0.221	-0.48	<0.001	0.938 ns	-1.575	-0.28	<0.001	0.557 ns
R8	-0.234	-0.45	<0.001	0.274 ns	-7.190	-0.55	<0.001	0.636 ns
R9	-0.370	-0.31	<0.001	0.304 ns	-3.602	-0.22	<0.001	0.427 ns
R10	-1.715	-0.48	<0.001	0.010*	-10.598	-0.55	<0.001	0.234 ns
R11	0.000	-0.03	0.690	0.110 ns	-4.130	-0.39	<0.001	0.361 ns
R12	-0.172	-0.13	0.045	0.349 ns	0.000	-0.11	0.102	0.040*
R13	-0.670	-0.30	<0.001	0.633 ns	0.000	+0.15	0.023	0.003**
R14	0.000	-0.09	0.191	<0.001***	-11.592	-0.52	<0.001	0.013*
R15	-0.144	-0.53	<0.001	<0.001***	-2.589	-0.44	<0.001	0.042*

[†]p-cor: p-value from Mann-Kendall test applied to detrended residuals, accounting for residual serial correlation. *** p<0.001, ** p<0.01, * p<0.05, ns not significant.

Chilean basins to precipitation along the latitudinal gradient.

E. Decadal Percentage Changes

Table III summarizes the decadal percentage changes in annual streamflow estimated using both the linear regression and Mann-Kendall methods. The results indicate consistent flow reductions across the northern regions (R1-R5), with mean losses of approximately 21% and 14% per decade, respectively. Central regions (R6-R11) exhibit smaller but still negative trends, suggesting a gradual decline in water availability. In contrast, the southern regions (R12-R15) show notable flow increases, particularly in regions R13 and R14, where gains exceed 25% and 55% per decade, respectively. This pronounced latitudinal contrast highlights the uneven impact of climatic forcing along Chile's territory, with a persistent drying trend in the north and central zones and potential intensification of hydrological regimes in the south.

F. Hovmöller Diagnostics

Fig. 7. presents the Hovmöller diagrams of 10-year mean precipitation and river flow across Chile for the period 1910-2015. These panels provide a clear visualization of the spatiotemporal evolution of both variables, highlighting the latitudinal gradient and long-term variability in hydroclimatic behavior. A persistent decrease in precipitation and streamflow is observed in the northern and central regions, particularly after the mid-20th century, whereas southern regions display a more stable or even increasing trend. The temporal coherence between both series suggests a strong climatic coupling, with precipitation variability acting as the primary driver of the observed hydrological patterns.

IV. DISCUSSION

From a methodological standpoint, the performance of the state-space Kalman smoother as a reconstruction tool was

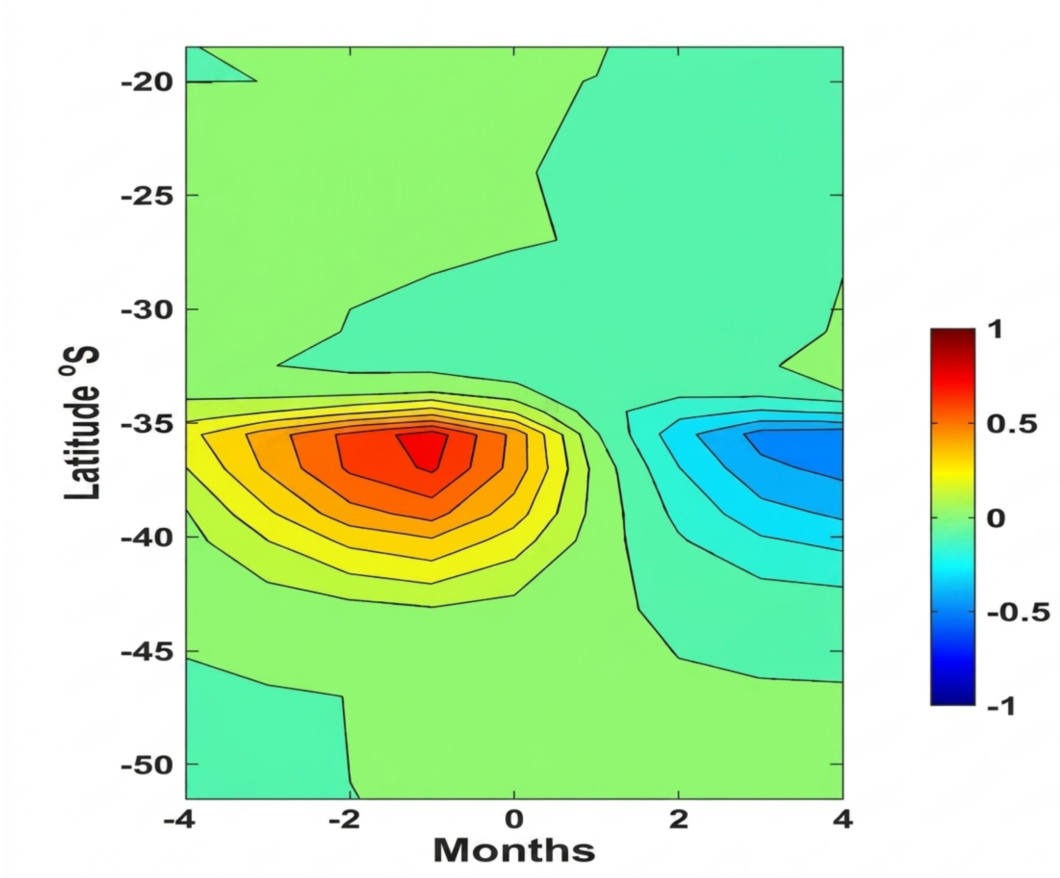

Fig. 6. Latitudinal cross-correlation between rainfall and river flow at monthly lags.

assessed through a block cross-validation experiment, in which up to three non-overlapping 12-month segments with complete observed data were withheld from each regional series and subsequently imputed using three deterministic baseline methods: linear interpolation, cubic spline interpolation, and seasonal mean substitution. The reconstruction accuracy of each method was quantified by the root mean square error (RMSE) and mean absolute error (MAE) between the withheld observations and the imputed values, with results summarized in Table IV.

Among the three baselines, the seasonal mean substitution approach yields the lowest global error ($RMSE = 31.31m^3/s$; $MAE = 26.42m^3/s$), outperforming linear interpolation ($RMSE = 37.29m^3/s$; $MAE = 31.53m^3/s$) and cubic spline interpolation ($RMSE = 56.45m^3/s$; $MAE = 48.59m^3/s$). The relatively strong performance of the seasonal baseline reflects the pronounced annual cycle present in Chilean river discharge, which a simple climatological mean can approximate reasonably well over short gaps. Linear interpolation performs best in the northern arid regions (R1-R5), where discharge variability is low and temporal gradients are smooth, whereas spline interpolation consistently underperforms across all regions, likely due to oscillatory artifacts generated over multi-month gaps in irregularly sampled series. In the high-discharge southern regions (R9-R13), all deterministic methods exhibit substantially larger errors, with RMSE values exceeding $45m^3/s$, underscoring the difficulty of reconstructing highly variable flows from local interpolation alone.

The Kalman smoother could not be directly evaluated within this short-window cross-validation framework, because the withheld 12-month blocks embedded in century-scale series with irregular station coverage did not provide sufficient contiguous data for stable likelihood optimization during the expectation-maximization fitting of the state noise variances. However, the cross-validation results serve an important comparative purpose: they establish the reconstruction skill achievable by deterministic methods operating on local temporal information alone, against which the structural advantages of the state-space approach can be assessed. Unlike all three baselines, the Kalman smoother simultaneously decomposes the observed series into level, trend, and seasonal components through a probabilistic generative model, propagates uncertainty across gaps of arbitrary length, and yields smoothed state estimates that are globally consistent with the full temporal structure of the series. These properties are directly relevant for the reliability of subsequent trend attribution: a seasonal mean imputation, for instance, introduces no artificial trend by construction, but it also fails to capture the evolving level and slope of the series, potentially biasing the reconstructed trajectory in periods of rapid change. The state-space framework avoids this limitation by treating the

TABLE III
DECADAL PERCENTAGE CHANGE IN ANNUAL STREAMFLOW BY REGION (REGRESSION VS MANN–KENDALL)

Region	ΔQ (% decade^{-1}, Linear Regression)	ΔQ (% decade^{-1}, Mann–Kendall)
1	-18.9332	-13.4997
2	+8.3807	+4.9572
3	-22.2969	-20.4791
4	-22.6412	-9.8598
5	-20.0049	-11.7218
6	-3.9787	-3.8733
7	-0.8709	-0.5153
8	-12.2923	-7.1049
9	-4.3687	-2.1779
10	-12.6493	-7.8002
11	-17.0874	-15.1514
12	+1.8970	+1.2984
13	+27.3855	+24.8899
14	+60.8500	+56.9027
15	+14.3823	+14.5393

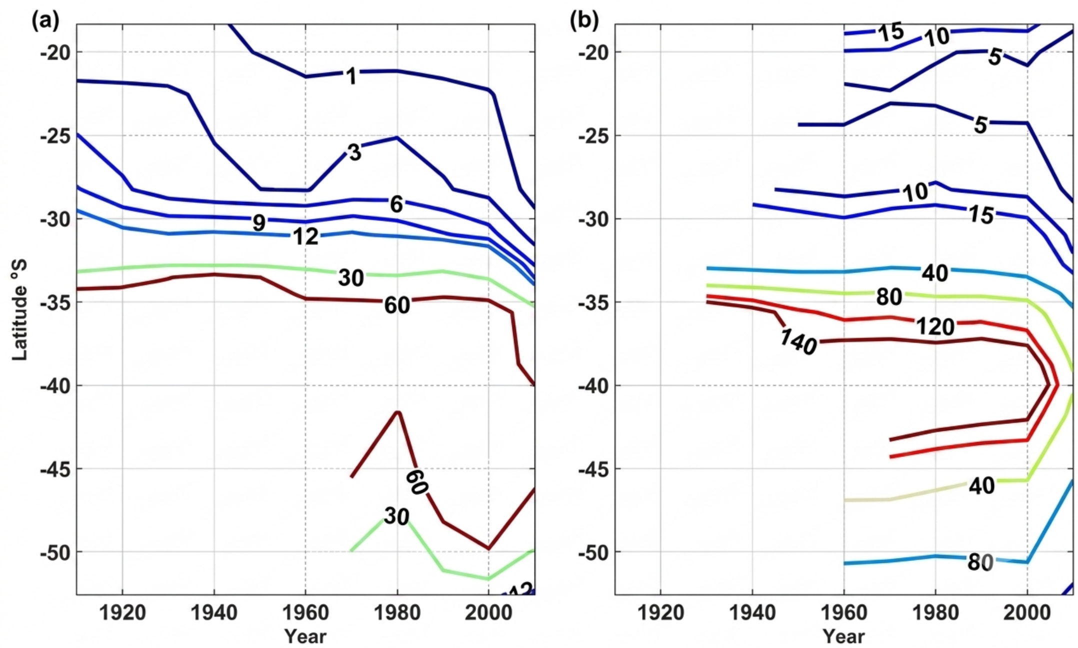

Fig. 7. Hovmöller diagrams of 10-year mean precipitation (a) and river flow (b) across Chile (1910–2015).

trend itself as a latent dynamic state updated continuously by the Kalman filter, ensuring that reconstructed values reflect the underlying hydroclimatic trajectory rather than a static climatological reference.

The coherence of results across methodological stages further reinforces confidence in the conclusions. The Kalman-reconstructed series, by filling gaps in a temporally consistent manner, reduces the risk of spurious trends arising from uneven station coverage over time – a limitation that would affect simpler imputation strategies. The cross-correlation results, showing stronger coupling in the south and weaker in the north, contextualize why trend magnitudes differ so markedly between regions: where precipitation drives discharge efficiently (high correlation, short lag), declining rainfall translates directly into declining flow. The Hovmöller diagrams visually confirm that this spatial pattern has been stable and progressive over decadal timescales, rather than a short-term fluctuation.

The long-term hydrological evolution revealed by this study shows a clear north-south asymmetry in both river discharge and precipitation across Chile. The combination of state-space modeling and classical trend detection techniques provides robust evidence of persistent drying in central and northern regions and a gradual intensification of river flows in the far south. These contrasting signals reflect Chile's strong climatic gradient and its sensitivity to large-scale atmospheric circulation patterns that modulate moisture transport along the Andes-Pacific corridor.

The results are consistent with recent hydrological evidence pointing to an intensification of drought conditions and a southward displacement of precipitation patterns, with detected downward trends aligning with spatial analyses based on both satellite and in-situ data [7].

The widespread negative trends identified by both OLS and Theil-Sen estimators between 30°S and 40°S are consistent with the well-documented decline in precipitation reported

TABLE IV
CROSS-VALIDATION RECONSTRUCTION ACCURACY BY REGION (MEAN RMSE AND MAE OVER WITHHELD 12-MONTH BLOCKS)

Region	RMSE Linear	RMSE Spline	RMSE Seasonal	MAE Linear	MAE Spline	MAE Seasonal
R1	0.78	1.53	0.68	0.70	1.35	0.49
R2	0.30	0.46	0.23	0.17	0.33	0.11
R3	0.88	0.80	1.83	0.61	0.58	1.71
R4	1.22	2.40	2.51	0.93	2.19	2.16
R5	1.85	6.55	3.92	1.50	5.90	3.49
R6	8.87	10.70	16.00	6.63	8.80	13.70
R7	17.10	31.80	8.39	12.30	26.80	7.20
R8	13.00	28.10	13.80	10.20	24.10	12.40
R9	55.40	112.00	38.70	52.80	104.00	32.40
R10	110.00	113.00	96.70	90.90	98.10	75.40
R11	120.00	181.00	70.00	99.90	151.00	59.20
R12	102.00	176.00	45.70	87.40	149.00	36.30
R13	62.10	82.10	73.60	51.10	67.60	64.40
R14	47.60	74.30	88.50	42.00	65.00	79.90
R15	18.20	26.40	9.09	15.90	23.60	7.38
Global mean	37.29	56.45	31.31	31.53	48.59	26.42

Units: m^3/s. RMSE = Root Mean Square Error; MAE = Mean Absolute Error. Baselines: Linear = linear interpolation; Spline = cubic spline; Seasonal = monthly climatological mean. The Kalman smoother could not be evaluated in the cross-validation blocks due to insufficient contiguous observations within withheld segments; see text.

over past decades [1], [2], [11]. Central Chile, in particular, has experienced recurrent droughts since the mid-20th century, culminating in the “megadrought" period of 2010-2015. The reduction in winter rainfall, coupled with rising temperatures, likely enhanced evapotranspiration and reduced snowpack accumulation, leading to diminished baseflows and lower annual discharges. The Mann-Kendall analysis applied here with a correction for residual serial correlation following Hamed and Rao [24], further confirms the statistical robustness of these downward trends in Regions R1, R2, R5, R6, R10, and R15, underscoring the persistence of hydroclimatic drying in the Mediterranean and subtropical zones. Importantly, the correction reveals that several central regions (R7-R9, R11-R13) lose significance once long-range serial dependence is accounted for, a result that highlights the importance of conservative inference in century-scale hydrological records with strong autocorrelation structure.

In contrast, southern Chile (south of 42°S) exhibits stable or positive flow trends, likely reflecting the increased influence of the Southern Westerlies and the poleward migration of westerly storm tracks. The strengthening of discharge in Regions R13-R15 aligns with reanalysis-based evidence of enhanced precipitation and runoff in high-latitude basins. This spatially coherent transition from negative to positive slopes suggests a progressive poleward displacement of the hydrological regime, with discharge isolines shifting approximately 1,200 km southward since 1950, as documented by the Hovmöller analysis.

The lagged cross-correlation analysis supports a strong coupling between rainfall and river flow, especially in the central and southern zones, where correlations peak at zero or short positive lags, indicating a near-immediate hydrological response consistent with the steep terrain and short catchment residence times. In the arid north, correlations weaken and shift toward longer lags, suggesting a combination of low runoff efficiency, groundwater buffering, and high evaporative demand. The progressive decline of precipitation and discharge in central Chile after 1950 coincides with documented shifts in the Pacific Decadal Oscillation (PDO) and increased occurrence of positive Southern Annular Mode (SAM) phases, which may have reinforced subtropical subsidence and reduced frontal system penetration, intensifying long-term water scarcity.

The implications of these findings are twofold. First, the detected drying in central Chile has direct consequences for water resources, agriculture, and hydropower generation, reinforcing the need for adaptive management under ongoing climate change. Second, the evidence of hydrological intensification in the south highlights the spatial redistribution of freshwater resources, which could alter ecosystem dynamics and flood regimes. Together, these findings underscore Chile’s vulnerability to large-scale climatic reorganization and the importance of integrated hydroclimatic monitoring at the national scale. These changes pose serious challenges for achieving water-related Sustainable Development Goals in Latin America (SDG 6, 13, and 15), particularly in regions where the energy sector depends on river flows for hydropower generation [26], and the integration of state-space models represents a valuable step toward resilient and adaptive management strategies.

Finally, several limitations should be acknowledged. The sparse early-century station coverage introduces uncertainty in regional reconstructions, particularly in northern basins. The regional aggregation strategy, while effective for characterizing large-scale latitudinal gradients, does not explicitly account for spatial dependence among neighboring regions; spatial autocorrelation arising from shared climatic drivers, orographic effects, and basin connectivity may influence both the reconstruction and the trend estimates. Spatiotemporal hierarchical models [27], [28] represent a natural extension of the present framework, as they can simultaneously estimate regional trends while borrowing strength across spatially correlated units. Future work should also incorporate remote sensing and reanalysis products to refine spatial resolution, assess non-linear dynamics, and extend the state-space framework to multivariate settings – including temperature, snow cover, and evapotranspiration – to further clarify the causal linkages driving the observed hydrological changes.

V. Conclusions

Prior to this study, no unified, century-scale assessment integrating river flow and precipitation trends across all 15 Chilean regions existed. Local or basin-specific analyses were unable to characterize the full latitudinal extent of hydroclimatic change, and the absence of a probabilistic reconstruction framework left long-term trend estimates vulnerable to bias from uneven and incomplete station records.

This study fills that gap. By applying a state-space time series model with Kalman filtering and smoothing to 604 streamflow and 831 precipitation stations over the period 1910-2015, we now know that Chile's hydrological system has undergone a statistically robust, spatially coherent, and decadally persistent reorganization that cannot be attributed to data artifacts or short-term variability.

The central finding is a pronounced north-south asymmetry. Central and northern Chile exhibit persistent drying and declining river flows, with the strongest and most statistically robust negative trends concentrated in Regions R1, R2, R5, R6, R10, and R15 after correcting for residual serial correlation using a conservative detrended Mann-Kendall approach. The most pronounced flow declines occur in Regions R9 (Maule, $\beta_1 = -0.463 m^3 s^{-1} yr^{-1}$), R10 (Biobío, $\beta_1 = -1.463 m^3 s^{-1} yr^{-1}$), and R11 (Araucanía, $\beta_1 = -1.154 m^3 s^{-1} yr^{-1}$), located in the Mediterranean-to-temperate transition zone. In contrast, Region R14 (Aysén) is the only region with a statistically significant positive flow trend ($\beta_1 = +4.328 m^3 s^{-1} yr^{-1}, p < 0.001$), while southern regions R13-R15 show stable or increasing discharge consistent with the poleward shift of westerly storm tracks.

Cross-correlation diagnostics reveal that the spatial gradient of trend magnitudes is mechanistically grounded: where precipitation drives discharge efficiently – high correlation at zero or short positive lag, as in central and southern regions – declining rainfall translates directly and rapidly into declining flow. In the arid north, weakened and delayed correlations reflect low runoff efficiency, groundwater buffering, and high evaporative demand, explaining why trend signals there are less spatially coherent despite significant long-term drying. The Hovmöller analysis confirms that the southward displacement of the main discharge zones, estimated at approximately 1,200 km since 1950, is a decadally stable and progressive structural shift rather than a transient fluctuation, consistent with large-scale circulation changes associated with the PDO and positive SAM phases.

These findings collectively establish that Chile's hydrological system is undergoing a climate-driven spatial redistribution of freshwater resources with direct consequences for water supply, agriculture, hydropower generation, and the achievement of water-related Sustainable Development Goals (SDG 6, 13, and 15). The results underscore the

urgency of adaptive water management strategies that explicitly account for the poleward migration of precipitation and discharge regimes.

Future extensions of this work should address three priorities. First, multivariate state-space formulations incorporating temperature, evapotranspiration, and snow cover would refine the mechanistic understanding of the causal pathways driving the observed trends. Second, spatiotemporal hierarchical models that borrow statistical strength across neighboring regions would improve uncertainty quantification in data-sparse northern basins. Third, integration with satellite-derived and reanalysis products would extend the spatial resolution of the reconstruction framework beyond the limitations of the ground-based station network, enabling non-linear and regime-shift dynamics to be assessed at finer scales across the Andean-Pacific domain.

Acknowledgments

The author gratefully acknowledges the General Directorate of Water (Dirección General de Aguas, DGA) for providing access to the data, the GI2611708 Project of the University of Bío-Bío, the Dean's Office of the Faculty of Health and Food Sciences (FACSA), the Directorate of Artistic Research and Creation (DICREA), and the Academic Vice-Rector's Office (VRA) of the same University for their support.

Data Availability

Data are publicly available at the DGA portal: https://snia.mop.gob.cl/dgasat/pages/dgasat_param/dgasat_param.jsp?param=1

References

[1] I. Fuentes, R. Fuster, D. Avilés, and W. Vervoort, "Water scarcity in central Chile: The effect of climate and land cover changes on hydrologic resources," *Hydrological Sciences Journal*, vol. 66, no. 6, pp. 1028–1044, 2021. https://doi.org/10.1080/02626667.2021.1903475

[2] P. Meseguer-Ruiz *et al.*, "General dry trends in Chile: Grid-based analysis 1979-2019," *Frontiers in Earth Science*, vol. 12, article 1355443, 2024. https://doi.org/10.3389/feart.2024.1355443

[3] D. Latoja, M. Lillo-Saavedra, C. Gonzalo-Martin, *et al.*, "Decadal variability of dry days in central Chile," *Earth System and Environment*, vol. 9, pp. 1117–1134, 2025. https://doi.org/10.1007/s41748-024-00526-6

[4] A. Montecinos and P. Aceituno, "Seasonality of the ENSO-related rainfall variability in central Chile and associated circulation anomalies," *Journal of Climate*, vol. 16, pp. 281–296, 2003. https://doi.org/10.1175/1520-0442(2003)016<0281:SOTERR>2.0.CO;2.

[5] M. I. Brunner, B. Hingray, M. Zappa, and A.-C. Favre, "Future trends in the interdependence between flood peaks and volumes: Hydro-climatological drivers and uncertainty," *Water Resources Research*, vol. 55, no. 6, pp. 4745–4759, 2019. https://doi.org/10.1029/2019WR024701

[6] J. A. Rutllant, H. Fuenzalida, and P. Aceituno, "Climate dynamics along the arid northern coast of Chile: The 1997-1998 Dinámica del Clima de la Región de Antofagasta (DICLIMA) experiment", *J. Geophys. Res. Atmos.*, vol. 108, D17, 2003. https://doi.org/10.1029/2002JD003357

[7] C. Álvarez-Garreton, J. P. Boisier, and R. D. Garreaud, J. Seibert, and M. Vis, "Progressive water deficits during multiyear droughts in basins with long hydrological memory in Chile", *Hydrology and Earth System Sciences*, vol. 25, pp. 429-446, 2021. https://doi.org/10.5194/hess-25-429-2021

[8] R. D. Garreaud, J. P. Boisier, R. Rondanelli, A. Montecinos, H. H. Sepúlveda, and D. Veloso-Aguila, "The Central Chile Mega Drought (2010-2018): A climate dynamics perspective," *International Journal of Climatology*, vol. 40, no. 1, pp. 421–439, 2020. https://doi.org/10.1002/joc.6219.

[9] A. Muñoz, A. González-Reyes, et al. "Streamflow variability in the Chilean Temperate-Mediterranean climate transition (35°S-42°S) during the last 400 years inferred from tree-ring records", *Climate Dynamics*. 47, 4051-4066, 2016. https://doi.org/10.1007/s00382-016-3068-947.

[10] IPCC, *Climate Change 2013: The Physical Science Basis*. Cambridge, U.K.: Cambridge University Press, 2014. https://doi.org/10.1017/CBO9781107415324

[11] N. W. Arnell and S. N. Gosling, "The impacts of climate change on river flow regimes at the global scale", *J. Hydrol.*, vol. 486, pp. 351–364, 2013. https://doi.org/10.1016/j.jhydrol.2013.02.010

[12] P. Döll, B. Jiménez-Cisneros, T. Oki, N. W. Arnell, G. Benito, J. G. Cogley, and A. Nishijima, "Integrating risks of climate change into water management," *Hydrol. Sci. J.*, vol. 60, no. 1, pp. 4–13, 2015. https://doi.org/10.1080/02626667.2014.967250

[13] Y. Hirabayashi, R. Mahendran, S. Koirala, L. Konoshima, D. Yamazaki, S. Watanabe, H. Kim, and S. Kanae, "Global flood risk under climate change," *Nat. Clim. Change*, vol. 3, no. 9, pp. 816–821, 2013. https://doi.org/10.1038/nclimate1911

[14] J. Durbin and S. J. Koopman, *Time Series Analysis by State Space Methods*, 2nd edn. Oxford, UK: Oxford University Press, 2012. https://doi.org/10.1093/acprof:oso/9780199641178.001.0001

[15] H. B. Mann, "Nonparametric tests against trend", *Econometrica*, vol. 13, no. 3, pp. 245–259, 1945. http://dx.doi.org/10.2307/1907187

[16] D. R. Helsel and R. M. Hirsch, K. R. Ryberg, S. A. Archfield, and E. J. Gilroy. *Statistical Methods in Water Resources*. Amsterdam, Netherlands: Elsevier, 2023. https://doi.org/10.3133/tm4A3

[17] P. K. Sen, "Estimates of the regression coefficient based on Kendall's tau," *J. Amer. Stat. Assoc.*, vol. 63, no. 324, pp. 1379–1389, 1968. https://doi.org/10.1080/01621459.1968.10480934

[18] R. Mendelssohn, "The STAMP software for state space models," *Journal of Statistical Software*, vol. 41, no. 2, pp. 1–18, 2011. https://doi.org/10.18637/jss.v041.i02

[19] W. Zhao and R. Prado, "Efficient Bayesian PARCOR approaches for dynamic modeling of multivariate time series," *Journal of Time Series Analysis*, vol. 41, no. 5, pp. 759–784, 2020. https://doi.org/10.1111/jtsa.12534

[20] R. Prado, M. A. R. Ferreira, and M. West, *Time Series: Modeling, Computation, and Inference*, 2nd ed. Boca Raton, FL: Chapman and Hall/CRC, 2021. https://doi.org/10.1201/9781351259422

[21] M. I. Brunner and L. Slater, "Future trends in river floods: An emerging hydrological-climatic typology," *Nature Reviews Earth & Environment*, vol. 2, pp. 681–694, 2021. doi: 10.1038/s43017-021-00223-1.

[22] A. Ramanathan, P. A. Versini, D. Schertzer, R. Perrin, L. Sindt, and I. Tchiguirinskaia, "Stochastic simulation of reference rainfall scenarios for hydrological applications using a universal multi-fractal approach", *Hydrology and Earth System Sciences*, vol. 26, pp. 6477–6491, 2022. https://doi.org/10.5194/hess-26-6477-2022

[23] J. Helske, "KFAS: Exponential family state space models in R," *Journal of Statistical Software*, vol. 78, no. 10, pp. 1–39, 2017. https://doi.org/10.18637/jss.v078.i10

[24] K. H. Hamed and A. R. Rao, "A modified Mann-Kendall trend test for autocorrelated data," *Journal of Hydrology*, vol. 204, no. 1-4, pp. 182-196, 1998. https://doi.org/10.1016/S0022-1694(97)00125-X

[25] S. Yue and C. Y. Wang, "Applicability of prewhitening to eliminate the influence of serial correlation on the Mann-Kendall test," *Water Resources Research*, vol. 38, no. 6, pp. 4-1–4-7, 2002. https://doi.org/10.1029/2001WR000861

[26] C. Escobar-Avaria, R. Fuster, K. Silva-Urrutia, C. Bauer, A. de la Fuente, "Understanding Conditioning Factors for Hydroelectric Development in Chile: Bases for Community Acceptance". *Sustainability*. 2022; 14(22):15224. https://doi.org/10.3390/su142215224

[27] Cressie, N. & Wikle, C.K. Statistics for Spatio-Temporal Data. Wiley, 2011.

[28] Gelfand, A.E. et al. Handbook of Spatial Statistics. CRC Press, 2010.

Francisco Novoa-Muñoz is a Full Associate Professor at the Universidad del Bío-Bío, Chile, where he has been a faculty member since 2000. He holds a PhD in Mathematics with specialization in Statistics and Operations Research from the Universidad de Sevilla, Spain (2013), a Master's degree in Agricultural Engineering from the Universidad de Concepción, and undergraduate degrees in Mathematical Engineering and Mathematics from the same institution. His research focuses on statistical simulation, goodness-of-fit testing, time series modeling, and biostatistics. He has authored and co-authored numerous articles in high-impact WOS-ISI indexed journals, including Axioms, Children, Ecological Modelling, Frontiers in Public Health, IEEE Latin America Transactions, Mathematics, Metrika, Plos One, and, among others. He has also published books on statistical testing and serves as a reviewer for several international scientific journals indexed in Web of Science. He is an active member of research groups in applied mathematics and measurement instrument construction at his institution, and participates in the doctoral program in Economics and Information Management, as well as master's programs in Mathematics and Statistics. Throughout his academic career he has supervised more than 40 undergraduate and graduate theses, taught across multiple disciplines including statistics, biostatistics, research methodology, and quantitative methods, and received consistently high student evaluation scores between 6.8 and 7.0 out of 7.0.